

ARTICLE OPEN



Enhanced antifouling and separation capabilities of polydopamine@Ce-MOF functionalized PES ultrafiltration membrane

Dana Kadadou^{1,2}, Thanigaivelan Arumugham^{1,2}, Lina Tizani¹ and Shadi W. Hasan¹

The need for antifouling membranes is substantial due to fouling's negative impact on the effectiveness and durability of ultrafiltration membranes. In recent times, Metal-Organic Frameworks (MOFs) have emerged as effective additives for crafting ultrafiltration (UF) membranes. However, to harness their benefits and mitigate their drawbacks, a well-considered approach is imperative. In this work, polyethersulfone (PES) UF membranes were tailored with polydopamine (PDA)-modified cerium (Ce)-MOF (PDA@Ce-MOF) to achieve satisfactory antifouling properties and to remove biological macromolecules such as bovine serum albumin (BSA) and humic acid (HA) from wastewater. The non-solvent induced phase separation (NIPS) method was used to simultaneously fabricate the membrane and modify it with different PDA@Ce-MOF concentrations ranging from 0.05 to 0.50 wt.%. Results showed significant improvements on the membrane's morphology, hydrophilicity, porosity and pore size at 0.10 wt.% loading of PDA@Ce-MOF. The synergistic effect of the PDA and Ce-MOF on the membrane improved the pure water flux ($337 \text{ L m}^{-2} \text{ h}^{-1}$) and filtration performance in the filtration of Bovine serum albumin (BSA) and humic acid (HA) reporting $145 \text{ L m}^{-2} \text{ h}^{-1}$ and 98% rejection, and $164 \text{ L m}^{-2} \text{ h}^{-1}$ and 88% rejection; respectively. Further, water-attracting functional moieties of PDA@Ce-MOF hindered the deposition of BSA protein on the membrane surface, resulting in an excellent flux recovery ratio (FRR) of ~87%, alongside mitigated irreversible fouling.

npj Clean Water (2024)7:7; <https://doi.org/10.1038/s41545-024-00302-z>

INTRODUCTION

Globally, surface waters are experiencing heightened risks of contamination and pollution due to the emergence of pollutants, natural organic substances, industrial agents such as heavy metal ions and dyes, as well as enduring organic contaminants¹. Membrane technology including ultrafiltration (UF) has been deployed for wastewater treatment and water purification over the past few decades to remove turbidity-causing particles, bacteria, macromolecules, etc². Because of its exceptional separation capabilities, continuous operational nature, compact design, and minimal energy usage, UF membrane technology has emerged as a viable substitute for traditional methods of wastewater treatment³. Polyethersulfone (PES) is widely used in the preparation of UF membranes due to its unique properties, including high thermal stability, mechanical strength, and chemical inertness⁴. However, the inherent hydrophobicity of PES poses a major drawback that adversely affects the membrane filtration capabilities. Throughout the filtration process, hydrophobic interaction forces lead to the entrapment of organic pollutants within the membrane pores, causing notable fouling through pore blockage⁵. As a result, the creation of hydrophilic membranes has arisen as a great option to mitigate membrane fouling⁶. In this regard, numerous efforts have been made to increase the wettability of PES membranes by blending with hydrophilic polymers⁷, grafting with hydrophilic monomers⁸, coating⁹, and embedding hydrophilic nanomaterials¹⁰. Among these methods, the preparation of mixed matrix membranes (MMMs) that include nanofillers such as metal oxide¹¹, graphene oxide (GO)¹², graphitic carbon nitride (g-C₃N₄)¹³, and metal-

organic frameworks (MOFs)¹⁴, etc., has proven effective in preventing fouling.

In recent years, significant focus has been directed towards metal-organic frameworks (MOFs), attributed to their versatile applications including catalysis, drug delivery, and membrane separation¹⁵. The coordination between the metal ion and organic ligand forms a highly porous MOF network structure, which offers tremendous advantages in terms of high surface area, tunable structure, and ease of functionalization¹⁶. MOFs have demonstrated the potential for improving hydrophilicity and filtration efficiency. For example, Al-Shaeli et al. reported enhanced hydrophilicity and permeability in membranes through modification with UiO-66-NH₂ MOF. The incorporation of UiO-66-NH₂ MOF within the membrane facilitated the creation of supplementary routes for efficient water molecule transport while hindering the adsorption of the BSA protein¹⁷. The study by Ren et al. focused on creating advanced UF membranes with enhanced decontamination and filtration performance. They developed a MIL- poly (vinylidene fluoride) (PVDF) multifunctional membrane with high MIL-53(Fe) loading. The resulting membrane showcased excellent methylene blue (MB) removal, steady permeability, and efficient filtration¹⁸. Top of Form

Rameesha et al. fabricated PVDF hybrid UF membranes with silver (Ag) loaded MOF-5 for enhanced permeation, antifouling and antibiofouling performance. These membranes demonstrated exceptional performance in terms of permeability, fouling resistance, and hydrophilicity. Notably, the PVDF/Ag@MOF-0.5 hybrid membrane showcased remarkable characteristics, including a high-water flux of 236.5 LMH, exceptional rejection rates (98.4% for bovine serum albumin (BSA), 96.5% for humic acid

¹Center for Membranes and Advanced Water Technology (CMAT), Department of Chemical and Petroleum Engineering, Khalifa University of Science and Technology, PO Box 127788 Abu Dhabi, United Arab Emirates. ²These authors contributed equally: Dana Kadadou, Thanigaivelan Arumugham. [✉]email: shadi.hasan@ku.ac.ae

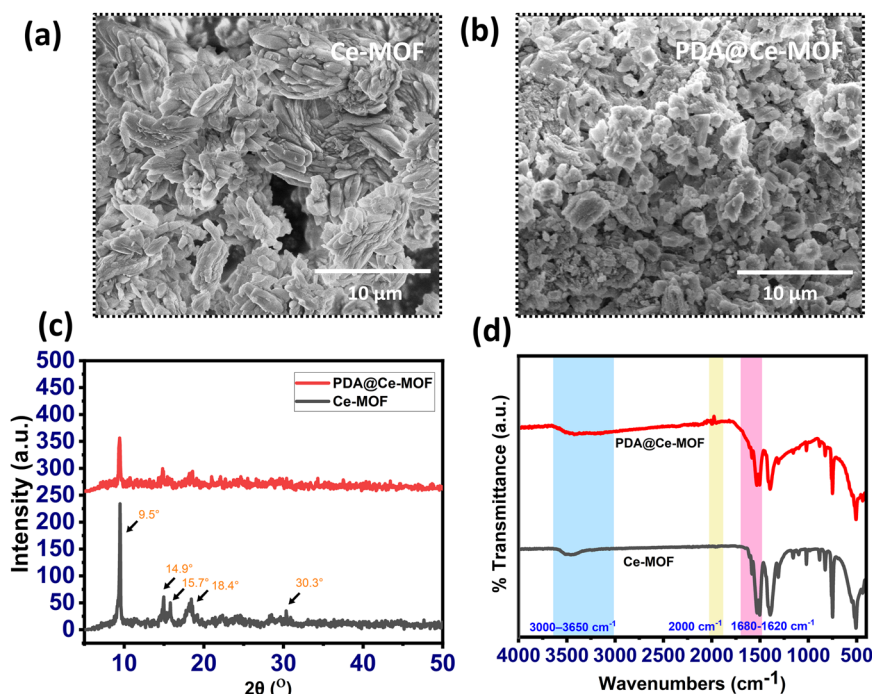


Fig. 1 Structure, XRD, and FTIR analysis of Ce-MOF and PDA@Ce-MOF. SEM images of (a) Ce-MOF and (b) PDA@Ce-MOF. (c) XRD, and (d) FT-IR images of Ce-MOF and PDA@Ce-MOF. The scale bars shown in a–b represent 10 μm , respectively.

(HA)), and robust antifouling properties (flux recovery ratio (FRR) of 89.7% for BSA, 92.4% for HA). Furthermore, PVDF/Ag@MOF-0.5 membranes exhibit outstanding antibacterial efficacy against both *E. coli* and *S. aureus*¹⁹.

Samari et al. developed a PES UF membrane by incorporating melamine-modified zirconium (Zr)-based UiO-66-NH₂ MOF. The modified membrane exhibited superior performance, manifesting reduced water contact angle and roughness, along with increased porosity compared to the base membrane. Introducing 0.1 wt.% MOF notably raised FRR from 59.2 to 95.22%²⁰. Tannic acid-modified hollow zeolitic imidazolate framework-8 (hZIF-8)/UF membrane possesses good mechanical, antifouling, and filtration capabilities²¹. Zhao et al. reported that Zn MOF-5@polydopamine modified UF membranes demonstrated high-water permeation capacity and BSA rejection of 209.02 LMH, and 99.12%; respectively²². Mohammadnezhad et al. introduced nanofiltration (NF) membranes containing lanthanides MOFs such as cerium (Ce)-MOFs for the removal of Direct Red 16. The modified membranes demonstrated high porosity and high-water permeation rates^{23,24}. Nevertheless, pure MOF materials have some limitations, including the hydrolysis of the metal-ligand bond over time, which threatens the stability of the MOF and compromises membrane performance²⁵. There are few studies reporting that MOF composites perform better than pure MOFs due to the easy availability of active functional groups²⁶.

Polydopamine (PDA) is also known as mussel-inspired “biogluce”. This environmentally friendly biopolymer can be produced by oxidizing dopamine (DA) under alkaline conditions. Due to its autooxidation nature, PDA can easily adhere to organic and inorganic surfaces, so it has received extensive attention in surface modification²⁷. Upon membrane modification with PDA, the incorporated catechol, imine, and amine functional groups enrich the hydrophilicity of the membrane surface²⁸. By modifying Ce-MOF surfaces with PDA, hydrophilic functional groups may be rendered, and PDA possesses inherent reducing properties, preventing Ce(III) from oxidizing to Ce(IV) and providing additional support for the Ce-MOF framework because of strong electrostatic

forces between the polymer chains and MOF²⁹. Therefore, “hydrophilic PDA” on “porous Ce-MOF” was expected to function as an effective surface modification agent for improving the filtration characteristics of the membrane³⁰.

This research introduces a new approach utilizing PDA modified Ce-MOF hybrid materials to create hydrophilic PES membranes via the phase inversion method. The recent literature survey revealed that no recent reports have been published on the modification of PES UF with a hybrid Ce-MOF so far. Through characterization including SEM, EDX, AFM, TGA, tensile strength, and contact angle analysis, we investigated the impact of PDA@Ce-MOF loading on membrane properties. Membrane permeation and separation performances were assessed using pure water flux, BSA and HA. Antifouling capability and membrane’s recyclability were evaluated through multiple cycles of BSA filtration. This study offers a fresh perspective on the advancement of MOF hybrid membranes for UF applications, introducing innovative methods to enhance membrane performance.

RESULTS AND DISCUSSION

Characterization of Ce-MOF and PDA@Ce-MOF

Figure 1a, b show the surface morphologies of Ce-MOF and PDA@Ce-MOF, respectively. Pure Ce-MOF exhibits elongated leaf (oblong)-like morphology, while PDA@Ce-MOF exhibits non-uniform morphology due to the surface coverage of PDA chains³¹. Supplementary Figure 1 shows the EDS elemental mapping images that illustrate how the functional groups are distributed within the Ce-MOF and PDA@Ce-MOF particles, respectively. While both particles have nearly identical elements, such as cerium, carbon, and oxygen, the PDA modification could provide an additional element, nitrogen, in the case of PDA@Ce-MOF. Additionally, the visual observation also confirms that the modification was successful, as the color change for the PDA@Ce-MOF was black. The recorded XRD spectrum for Ce-MOF and PDA@Ce-MOF in the range of $2\theta = 5^\circ\text{--}50^\circ$ is shown in

Fig. 1c. The characteristic XRD peaks at $2\theta = 9.5^\circ, 14.9^\circ, 15.7^\circ, 18.4^\circ$, and 30.3° are crystalline and confirm the formation of a Ce-MOF phase, which is in accordance with previous literature³². The peak intensity of PDA@Ce-MOF is lower than that of the XRD spectrum of Ce-MOF. However, no peaks are observed that correspond to PDA. The results suggest that Ce-MOF retains its stability even after modification, despite changes in its morphology (Fig. 1a). The FTIR spectra of Ce-MOF and PDA@Ce-MOF are shown in Fig. 1d. Ce-MOF displays two sharp peaks at 1571 and 1390 cm^{-1} , which correspond to coordinated carboxylic function groups³³. Next, the peaks at $3340, 1620, 1500,$ and 1287 cm^{-1} are attributed to the vibrational modes of O-H, N-H, C=O, C=C, and C-O in PDA³⁴.

Supplementary Figure 2 illustrates the changes in zeta potential values for Ce-MOF before and after PDA modification. A Ce-MOF matrix with the least amount of free carboxylic acid group yields a zeta potential of -1.8 mV ³⁵. After PDA modification, PDA@Ce-MOF surface is fully covered with oxygen-containing functional groups because of electrostatic interaction between Ce^{3+} and negatively charged oxygen (-OH and -COOH). As a result, after PDA modification, oxygen moieties provide negatively charged surfaces (for PDA@Ce-MOF particles), resulting in a decrease in zeta potential from -1.8 to -5.6 mV ³⁶.

According to Supplementary Fig. 3a, b, the specific surface areas of Ce-MOF and PDA@Ce-MOF are $161.9\text{ m}^2\text{g}^{-1}$ and $400.7\text{ m}^2\text{g}^{-1}$, respectively. Incorporating PDA onto Ce-MOF resulted in an increase in total pore volume from 0.14 to 0.35 cc/g . Nevertheless, the pore size is not significantly affected as both Ce-MOF and PDA@Ce-MOF showed similar low pore diameters of around $\sim 1.8\text{ nm}$ and pore size distributions ranging from 1.4 to 12.5 nm (refer to Supplementary Fig. 3c, d). Thus, the high specific surface area and pore volume indicate that Ce-MOF has been successfully modified by PDA. Supplementary Fig. 4 demonstrates the TGA spectrum of the Ce-MOF and PDA@Ce-MOF. The decomposition of water and coordinated BDC ligand molecules in this Ce-MOF resulted in a four-stage thermal degradation pattern³⁵. However, the TGA curve shows a steep decline after PDA modification due to the rapid degradation of PDA chains³⁵. Therefore, all results provide evidence that the PDA was successfully tethered to the Ce-MOF.

Surface morphology and EDS analysis of fabricated membranes

The top, cross-section, and bottom surfaces of all membranes are shown in Fig. 2. All membranes displayed smooth top surfaces, asymmetrical cross-sectional morphologies with inclined finger-like pores, and porous bottom surfaces. The modified membrane exhibited a highly interconnected porous morphology as compared to the bare membrane. It might be caused by the rapid movement of hydrophilic PDA@Ce-MOF particles towards the top surface during membrane formation. Further, the hydrophilic PDA@Ce-MOF particles could affect the kinetic and thermodynamic stability of the dope solution during the phase inversion step to facilitate solvent-non-solvent exchange resulting in longer, and larger pore nuclei (inclined finger-like channels) being formed²². Therefore, the modified membrane has a larger pore size and porosity than the pristine membrane (as discussed in Section 3.2.3.). Moreover, EDS mapping images shown in Supplementary Fig. 5 demonstrate the migration of hydrophilic PDA@Ce-MOF to the membrane's top selective layer during membrane formation. In the mapping images, it is evident that cerium and nitrogen are present in the modified membrane, which are not present in the PES pristine membrane.

Membranes surface roughness, porosity, pore size and mechanical properties

The three-dimensional (3D) AFM images of the pristine and PES/PDA@Ce-MOF modified membranes are shown in Fig. 3, which

represents the topology of the membrane surfaces. It is visible in the AFM images that the lighter and darker areas of the membrane surface correspond to the crests and troughs. Roughness is determined by the height difference between the peaks and valleys, which affects fouling behavior by either adsorption or desorption³⁷. Further, the calculated root mean square (RMS) roughness is shown in Supplementary Fig. 6. Surface roughness was found to be high for pristine M-0 membranes ($7.97 \pm 0.26\text{ nm}$). However, surface roughness values decreased with the addition of PDA@Ce-MOF up to $0.01\text{ wt.}\%$ to the membrane. The surface roughness value for M-0.10 decreased by 24% . When the addition of PDA@Ce-MOF materials exceeds $0.10\text{ wt.}\%$, the membrane surface roughness gradually increases. Because of the higher loading of the particles, agglomeration can result in an uneven dope solution³⁸. However, these values are still lower than those of the pristine M-0 membrane.

Pore size and porosity results are displayed in Fig. 4a. It is important to note that these results are consistent with our previous SEM and AFM results (see Figs. 2 and 3). Until $0.10\text{ wt.}\%$ PDA@Ce-MOF loading, the membrane's porosity, and pore size exhibit a positive trend due to the fastest solvent-non-solvent exchange process during membrane formation. M-0.10 exhibits a pore size of $\sim 45\text{ nm}$ and a porosity of $\sim 62\%$. When PDA@Ce-MOF addition exceeded $0.10\text{ wt.}\%$, the solution viscosity possible increased, resulting in a decrease in the membrane's pore size and porosity³⁹.

A tensile strength test was performed on the prepared membranes to evaluate their mechanical properties. Figure 4b shows the tensile stress-strain curve of all prepared membranes. The modified membrane demonstrated excellent tensile strength compared to the bare membrane (Supplementary Table 1). It was particularly evident that when the PDA@Ce-MOF particle loading increased from 0 to $0.1\text{ wt.}\%$, the membranes' tensile stress increased from 3.0 ± 0.2 to $3.7 \pm 0.2\text{ MPa}$; respectively. The uniform distribution of the PDA@Ce-MOF enhanced the mechanical properties of the M-0.10 membrane by $\sim 18\%$ compared to pristine PES membranes. Due to the intermolecular forces between the PDA@Ce-MOF and PES chains, the PDA@Ce-MOF dispersed uniformly in the membrane matrix restricts the free movement of polymeric chains by allowing twisting. Consequently, increasing membrane porosity did not have a significant effect on mechanical properties. A similar observation was noted in a previous study⁴⁰. However, PDA@Ce-MOF loadings exceeding $0.1\text{ wt.}\%$ degraded the tensile properties of the membranes due to the non-uniform dispersion of the particles⁵. The M-0.50 membrane results in a significant decrease in tensile strength, which is $\sim 7\%$ lower than the pristine membrane.

Membranes hydrophilicity, zeta potential (ζ) analysis and pure water flux

A contact angle analysis was performed at liquid-solid interfaces to assess the wettability of membranes. Figure 5a shows the contact angles for pristine and modified membranes. Because of the inherent hydrophobic nature of pristine PES materials, the M-0 membrane demonstrated a higher contact angle value of $76.9 \pm 0.9^\circ$. The higher contact angle was significantly reduced when the membrane was modified with PDA@Ce-MOF particles. The lowest contact angle of $61.1 \pm 0.2^\circ$ has been observed for M-0.50. By modifying the membrane surfaces with hydrophilic functional groups, such as hydroxyl groups from PDA and carboxylic acids from Ce-MOF, water molecules can form strong hydrogen bonds with the membrane surfaces. According to Fig. 5a, the calculated surface free energy of modified membranes is higher than that of pristine M-0 membrane. This high value of surface free energy represents a membrane surface that is more conducive to wetting, thus improving filtration and fouling resistance properties.

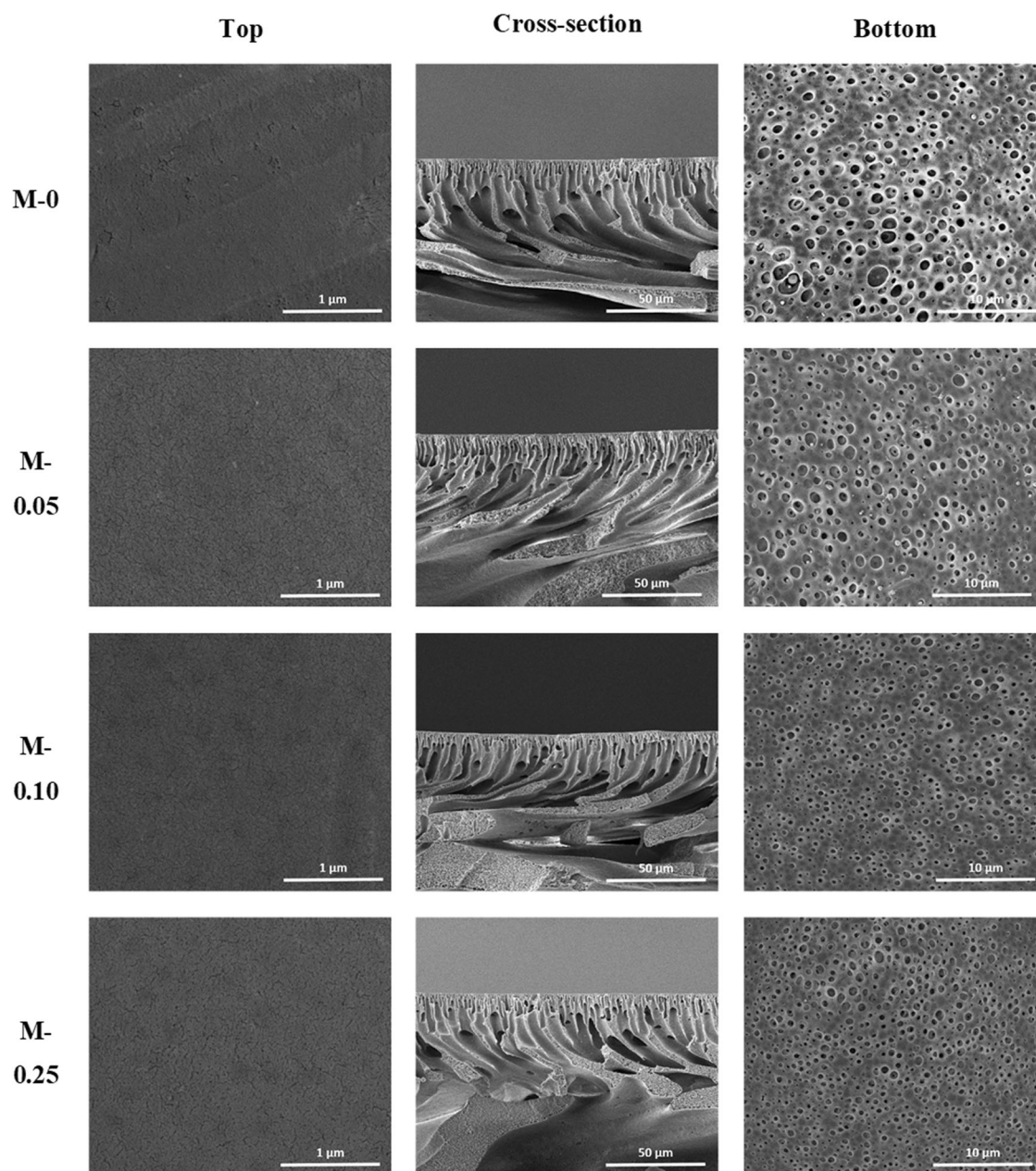


Fig. 2 Morphological analysis of the membranes. SEM micrographs display the top, cross-section, and bottom morphologies of the pristine and PES/PDA@Ce-MOF modified membranes. The scale bars (M-0 to M-0.50) in the top, cross-section, and bottom images represent 1 μm, 50 μm, and 10 μm, respectively.

As shown in Fig. 5b, the surface charge properties of the membranes (M-0 and M-0.10) were measured at different pH ranges between 5 and 9. Compared to bare membrane M-0, M-0.10 showed a high negative zeta potential value at all pH levels. In the case of increasing pH from 5 to 9, the negative zeta potential values of M0.1 increased from $-19.6 (\pm 0.5)$ to $-41.0 (\pm 0.3)$. It is notable that this high negative zeta potential value is ~ 1.6 times greater than M-0. Possibly the high negative zeta potential of M-0.10 may be due to the exceptional surface coverage provided by hydrophilic functional groups such as the hydroxyl and carboxylic functional groups from PDA@Ce-MOF⁴¹. As can be seen from Supplementary Fig. 7, PDA plays an important role in improving the surface charge. In the absence of PDA, the negative zeta potential of PES/Ce-MOF was only $-30 (\pm 0.2)$ at pH = 7. This

finding is also supported by our previous results regarding contact angles (refer to Fig. 5a).

Figure 5c clearly displays that as the concentration of PDA@Ce-MOF within the membrane matrix increased, a significant increase in pure water flux was observed. Increasing the PDA@Ce-MOF loading from 0 to 0.10 wt.% enhanced the pure water flux by 83%. However, there was a higher flux in M-0.25 than in M-0.10 regardless of the low porosity. Due to its high content of PDA@Ce-MOF, it readily accumulates on the top surface of the membrane and forms larger pores by creating a strong affinity between its hydrophilic groups (hydroxyl and carboxylic groups) and the water molecules⁴². This has a positive influence on the permeability of M-0.25, but not on M-0.50. While the membrane-modified Ce-MOF alone only improved flux by 29% compared with the pure

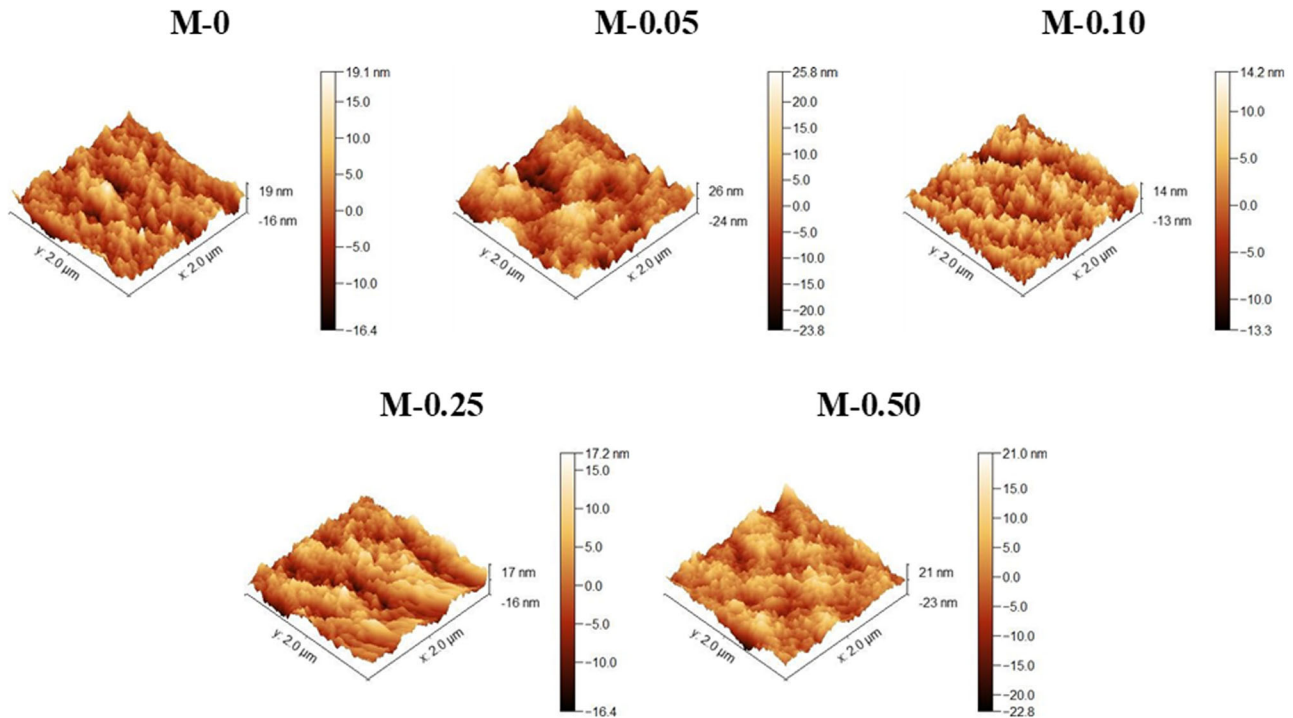


Fig. 3 AFM surface topological analysis of the membranes. AFM images of the membranes showing their 3D structures.

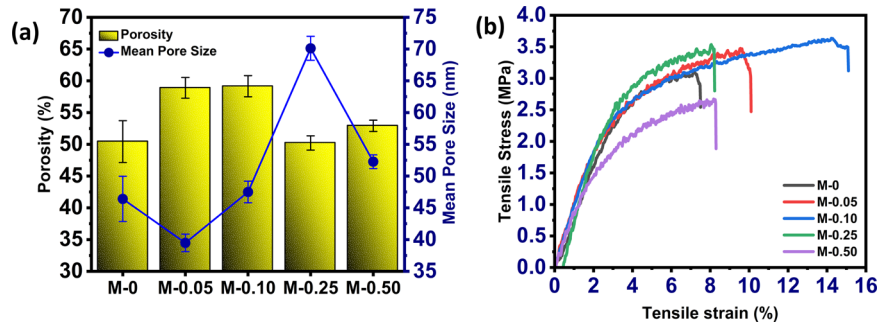


Fig. 4 Porosity, mean pore size, and mechanical properties of the membranes. **a** Porosity and mean pore size, and **(b)** mechanical properties of the prepared membranes; error bars present standard deviations, $n = 3$. The scale bars (M-0 to M-0.50) represent <25 nm.

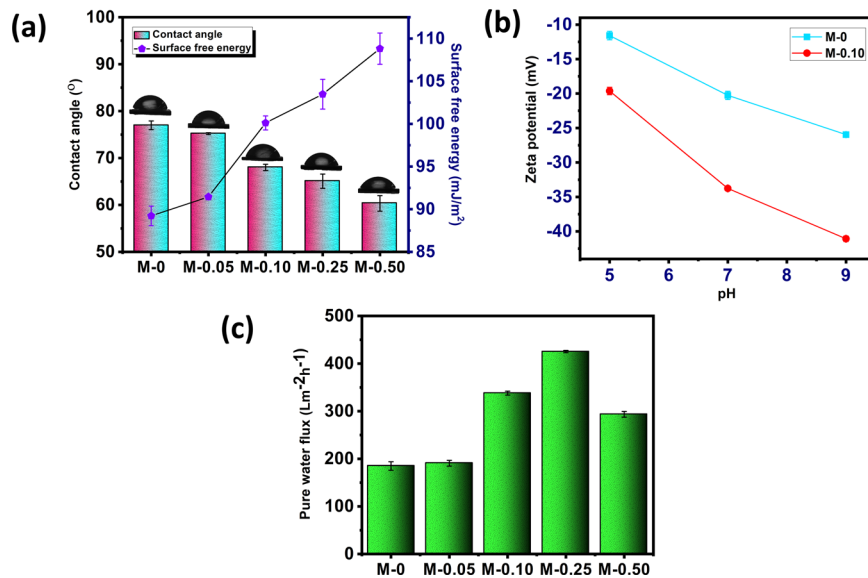


Fig. 5 Hydrophilicity, zeta potential, and pure water flux of the membranes. **a** Contact angle and surface free energy, **(b)** zeta potential, and **(c)** pure water flux of the prepared membranes; error bars present standard deviations, $n = 3$.

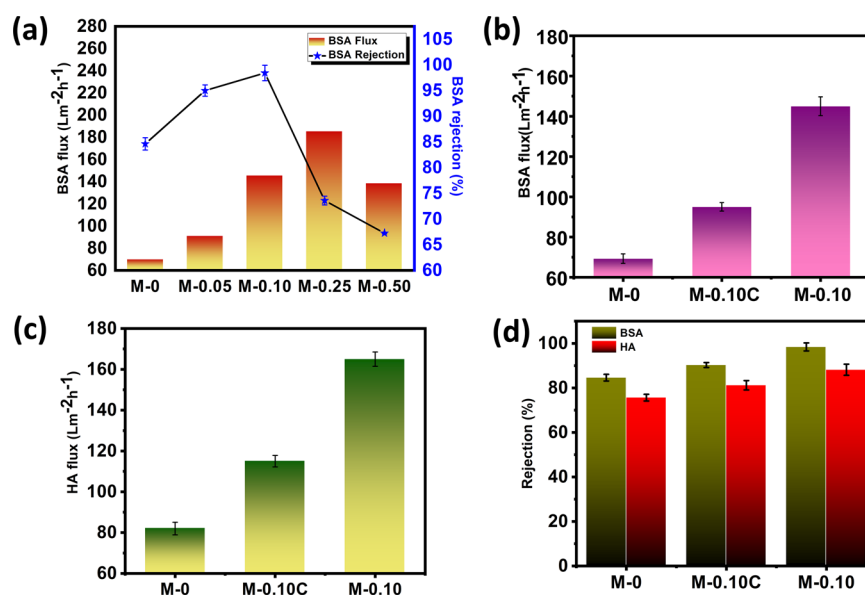


Fig. 6 Separation performance of the membranes. Filtration performances of the membranes towards (a, b) BSA and (c, d) HA ; error bars depict standard deviations, $n = 3$.

membrane, this value was 54% less than PES/PDA@Ce-MOF (M-0.10) (refer to Supplementary Fig. 8). Finally, according to the improvement in pure water flux results, large pore sizes, high porosity, and hydrophilicity contribute significantly to the facilitation of water transport across membrane (M-0.10) structure.

Membrane separation performance

Figure 6 shows the results of filtration tests conducted on the pristine and PES/PDA@Ce-MOF modified membranes against BSA and HA solutions having initial concentrations of 100 ppm and 50 ppm, respectively. First, all the modified membranes with PDA@Ce-MOF particles exhibited higher permeation to the prepared BSA solution (Fig. 6a). Especially, M-0.10 and M-0.25 membranes with 0.10 and 0.25 wt.% PDA@Ce-MOF loading exhibited the highest BSA permeation of 145.6 ± 4.7 LMH and 185.8 ± 4.0 LMH; respectively, leading to ~ 2.1 and ~ 2.6 times enhancement when compared to the M-0 pristine membrane. High permeation of the membranes could be explained by an increase in their hydrophilicity. Moreover, the BSA permeation results were consistent with those obtained in pure water flux, as shown in Fig. 5c. Both BSA permeation and BSA rejection increased for PDA@Ce-MOF loaded membranes until 0.10 wt.%. The performance of BSA rejection decreases significantly when the PDA@Ce-MOF concentration exceeds 0.10 wt.% due to the abrupt increase in mean pore size (Fig. 4a). The M-0.10 membrane showed the highest BSA rejection of $98.4 \pm 4.9\%$ at 0.10 wt.% PDA@Ce-MOF loading. A comparison of the HA solution filtration results of the pristine, M-0.10C and M-0.10 was performed, and the results are shown in Fig. 6b–d. M-0.10 performed well in the filtration of Bovine serum albumin (BSA) and humic acid (HA), with $145 \text{ L m}^{-2} \text{ h}^{-1}$ and 98% rejection, and $164 \text{ L m}^{-2} \text{ h}^{-1}$ and 88% rejection, respectively. It was apparent that membrane with PDA-modified Ce-MOF demonstrated better filtration performance against BSA and HA solutions due to the low contact angle, high porosity, and larger pore size.

Antifouling characteristics of the membranes

To assess the antifouling properties of the membranes, BSA solution and pure water were filtered cyclically for up to five cycles. In Fig. 7a, the cyclic filtration test results are presented for

M-0, M-0.10 C, and M-0.10. As shown in Fig. 7a, the integrated flux profile, the BSA flux is generally lower than the pure water flux due to the interaction between the BSA molecules and the membrane surface during filtration. Following five cycles, M-0.10 continues to exhibit superior filtration performance than pure membrane (M-0). During filtration, BSA molecules do not easily attach to smooth hydrophilic membrane surfaces, thereby not causing an abrupt reduction in flux. Furthermore, based on the flux profile, FRR values were calculated and displayed in Fig. 7b. The pristine membrane (M-0) has a FRR of 84.3% during cycle 1, but drops to 46.7% during cycle 5. Because the M-0 has a rough surface with hydrophobic properties, it has a higher tendency to attract foulants, which do not easily detach. Therefore, the drop in the FRR for the M-0 was significant. In contrast, when the membrane was modified with MOFs, the FRR remained high (Fig. 7b). The FRR values for PES/Ce-MOF (M-0.10C) membrane and PES/PDA@Ce-MOF (M-0.10) membrane was 78.4 and 87.9%, respectively, after five cycles of filtration. High FRR is a direct result of improved hydrophilicity, which increases antifouling ability.

According to Fig. 7c, irreversible and total fouling significantly decreased for modified membranes. When the number of filtration cycles is increased, R_{ir} and R_t of the pristine membrane (M-0) are observed to increase. Although MOF modified membranes also showed an increasing trend for R_{ir} and R_t during filtration cycles, the increase was not substantial enough to cause severe pore plugging. M-0.10 C and M-0.10 showed irreversible fouling ($R_{ir}, \%$) of $6.3 (\pm 2.3)$ and $4.1 (\pm 2.2)$ at cycle-1 and $21.6 (\pm 1.7)$ and $12.1 (\pm 2.1)$ at cycle-5, respectively. The reason for the less fouling effect of PDA@Ce-MOF membrane could be in terms of surface charge, as the hydroxyl and carboxylic functional groups in PDA@Ce-MOF particles change the PES membrane to be negatively charged, maintaining the repelling force against the BSA molecule during filtration (refer to Fig. 5b). Therefore, loosely bound BSA molecules increase fouling in a reversible manner (refer to Fig. 7c). The reversibly fouled membrane is easy to clean due to the foulant accumulation only on the membrane surface or the weak interaction between the foulant and the membrane pores. In addition, a comparison of SEM images of the membrane surface before and after 5 cycles of BSA filtration is shown in Fig. 7d. Membrane M-0 exhibited uneven and significant

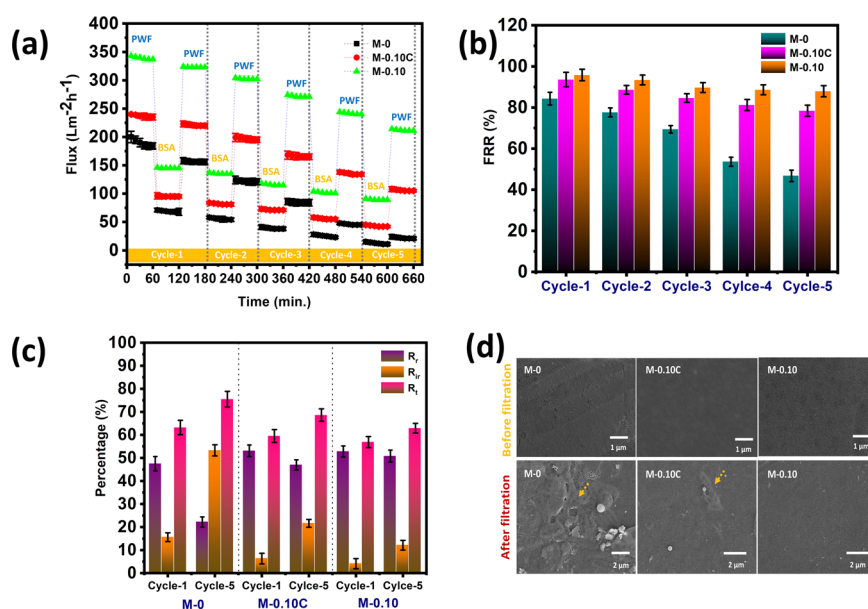


Fig. 7 Antifouling assessment of pristine and PDA@Ce-MOF modified membranes. **a** Integrated flux profiles **(b)** Flux recovery ratios (FRR) **(c)** reversible, irreversible, and total fouling (cycle 1 and 5) of all prepared membranes, and **(d)** SEM images of membranes before and after five cycles of BSA filtration; error bars depict standard deviations, $n = 3$.

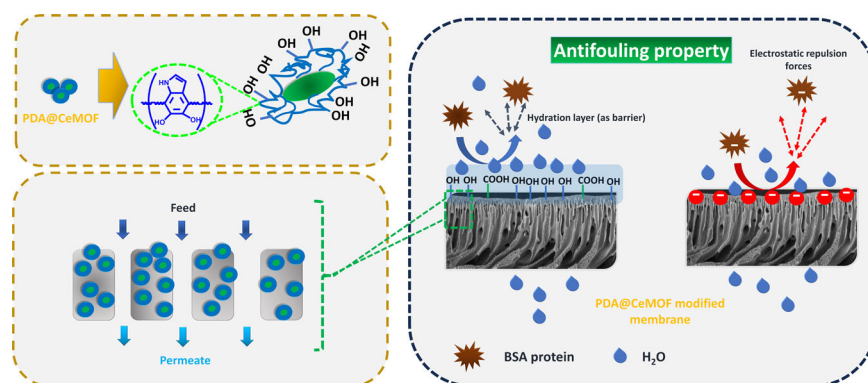


Fig. 8 Proposed separation mechanism of PDA@Ce-MOF modified membrane. Schematic depiction of the antifouling mechanisms of the PES/PDA@Ce-MOF UF membrane.

deposition of BSA fouling, whereas PDA@Ce-MOF modified membranes did not exhibit any significant differences.

Further, the antifouling mechanism of M-0.10 has been elucidated using surface roughness, contact angle, and zeta potential results. In detail, hydrophilic functional groups, such as the hydroxyl and carboxylic acid groups from PDA@Ce-MOF, are present on the membrane surface. These water-attracting functional groups create a hydration layer to facilitate foulant desorption during cleaning. Finally, hydrophilicity and a negative charge endow the PES membranes (M-0.10) with a strong antifouling ability (Fig. 8). In Table 1, the best-performing membrane, M-0.10, is compared with previous literature reports. The reported M-0.10 membrane in this study performed better and was comparable in terms of permeation, rejection, and antifouling properties.

METHODS

Materials

PES granules (M_w : 58 kDa), polyvinylpyrrolidone (PVP) (M_w : 10 kDa), N-N dimethylacetamide (DMAc), cerium (III) acetate

hydrate, 1,4-benzenedicarboxylic acid, Triethylamine (TEA), dimethylformamide (DMF), dopamine hydrochloride (DA), Trizma® hydrochloride (THCl) (>99.0%), sodium dihydrogen phosphate, sodium phosphate dibasic, BSA, and HA were all purchased from Sigma-Aldrich. Deionized (DI) water (resistivity: 15 $\text{M}\Omega\cdot\text{cm}$ at 25 °C), obtained from a Millipore Elix® Advantage 10 purification system (Millipore Corp., USA), was used throughout this study.

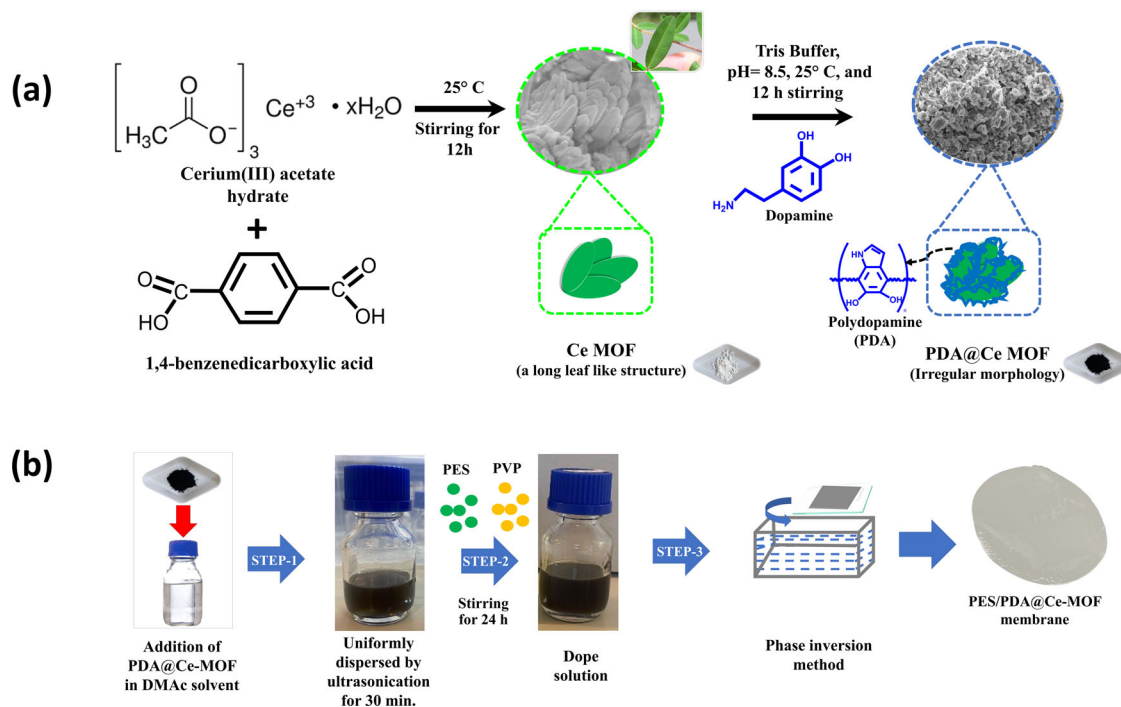
Synthesis of cerium metal-organic framework (Ce-MOF)

Ce-MOF was prepared using a method previously described⁴³, albeit with certain adjustments. Initially, cerium (III) acetate hydrate and 1,4-benzenedicarboxylic acid (BDC) were individually dissolved in 30 mL of water (designated as solution A) and 30 mL of dimethylformamide (DMF, referred to as solution B). After stirring for 30 min, solution B (the linker solution) was introduced cautiously into solution A using a glass dropper, employing a dropwise approach. Triethylamine (TEA) at a concentration of 0.001 M was incorporated as a modulating agent. For the solution blends, ultrasonication was conducted for 30 min, followed by 12 h of stirring at room temperature. The resultant Ce-MOF precipitate was collected by centrifugation and subsequently

Table 1. Comparison of PES/PDA@Ce-MOF UF membrane performance.

Membrane materials	Application	WCA, pristine/modified (°)	Water Flux, pristine/modified (LMH)	Rejection (%)	Antifouling properties (FRR %), pristine/modified	Ref.
PES/Ce-anthranilic acid MOF	Natural organic substances and whey wastewater	64/~48	5/30	99% of ^a COD, ^b BOD, ^c TSS and turbidity	34/70	46
PES/Ce-MOF	Powder milk solution	63/57	14.7/21.2	99% of direct Red 16	62.2/91.5	24
Melamine modified Zr-MOF	Milk powder	~76/61	44/49	99.7% of humic acid	59/95	20
Cellulose acetate/Cu MOF/PES	BSA protein and HA	75/46	21.9/28.5	79% HA 85% BSA	---	47
PES/PDA@Ce-MOF	Organic substances (BSA and HA)	77/66	184/337	98% BSA 88% HA	~46 / ~87 for BSA (Cycle-5)	This work

^aCOD chemical oxygen demand.
^bBOD, biochemical oxygen demand.
^cTSS, total suspended solids.

**Fig. 9 Nanomaterial synthesis and membrane fabrication schematics.** Schematic illustration of (a) PDA @Ce-MOF synthesis process, and (b) fabrication steps of PES/PDA@Ce-MOF membranes.

washed with DMF, water, and ethanol. Following the washing steps, the precipitate was subjected to drying in a hot air oven at 60 °C for 24 h. The final product, characterized by its white color, was stored in sterile sample tubes for subsequent analysis.

Preparation of PDA@Ce-MOF particles

A solution was prepared by dispersing 300 mg of Ce-MOF and 300 mg of DA in 300 mL of tris buffer (10 mM, pH 8.5) using ultrasonication for 15 min. Subsequently, the mixture was subjected to overnight stirring at room temperature with a stirring speed of 600 rpm. This facilitated the in-situ synthesis of PDA, which immobilized onto the Ce-MOF. After 24 h, the resulting black PDA@Ce-MOF powder was subjected to multiple washing cycles using distilled water through centrifugation at

8000 rpm. Upon washing, the wet powder was dried overnight at 60 °C. Figure 9a depicts the outlined process of Ce-MOF modification with PDA, showcasing visual representations of Ce-MOF prior to and subsequent to the modification procedure.

Fabrication of PES/PDA@Ce-MOF membranes

As shown in Fig. 9b, asymmetric pristine and PES/PDA@Ce-MOF UF membranes were fabricated using the nonsolvent-induced phase separation (NIPS) method⁴⁴. A set of five casting dope solutions were prepared using different compositions of PDA@Ce-MOF including 0, 0.05, 0.10, 0.25, and 0.50 wt.% in DMAc while maintaining PES and PVP at 18 and 1.0 wt.%, respectively. Table 2 shows the nomenclature and compositions of the fabricated pristine and PES/PDA@Ce-MOF nanocomposite membranes. At

Table 2. Composition of pristine and PES/PDA@Ce-MOF membranes.

Membrane	PES (wt.%)	PVP (wt.%)	PDA@Ce-MOF (wt.%)	DMAc (wt.%)
M-0	18	1.0	0	81
M-0.05	18	1.0	0.05	80.95
M-0.10	18	1.0	0.10	80.9
M-0.25	18	1.0	0.25	80.75
M-0.50	18	1.0	0.50	80.5

first, the PDA@Ce-MOF were dispersed in the specified amounts of DMAc using ultrasonication baths for 30 min. Then, PVP and moisture free PES granules were added slowly to the DMAc solutions while stirring at 200 rpm at 50 °C. The solutions were then left to stir uninterruptedly. After 24 h, the solutions were left to degas using sonication and a vacuum oven for 20 min and 3 h at 25 °C; respectively. The dope solutions were then cast on clean glass plates using a flat-sheet casting machine (Elcometer 4340) and a casting blade with a gate height of 200 μm at ambient conditions. The phase inversion process was then immediately initiated by immersing the PES film-coated glass plates in a coagulation bath containing distilled water at room temperature. The membranes were then left in the coagulation baths overnight to ensure full phase separation. Following the membrane fabrication step, the membranes were thoroughly washed with deionized water to remove any residues of the DMF solvent and PVP additives, and then they were stored in deionized water until they were tested or characterized. As a further evaluation of PDA modification on Ce-MOF, PES/Ce-MOF (0.1 wt%) membranes without PDA were prepared and labeled as M -0.10 C (refer to Supplementary Fig. 9).

Characterization of PDA@Ce-MOF particles

Field emission gun (FEG) SEM, Quanta FEG 250 (FEI, Oregon, United States), coupled with energy dispersive system (EDS), was utilized in this study. The morphology and elemental composition of the PDA@Ce-MOF particles were examined. Prior to morphological and elemental analysis of the samples, a 7 nm layer of gold was deposited on the surface of the samples to maximize conductivity and enhance SEM analysis. The imaging was conducted under a 5 kV accelerating voltage with a working distance of 10 mm. X-ray diffraction (XRD) analysis was performed using Bruker D2 Phased XRD diffractometer to determine the crystallinity of the samples at a current of 10 mA, voltage of 30 kV, and a wavelength of 1.5418 Å in a 2θ range of 5° to 50°. The data was acquired at a scanning rate of 0.05° s⁻¹. Moreover, the functionalization of the MOF was confirmed with Bruker ATR FTIR, VERTEX 80 v (Bruker, Massachusetts, United States). Specific surface area, pore volume, and pore size of the MOF samples was calculated from N₂ adsorption-desorption isotherms at 77 K using a Quantachrome nova 2200e instrument. The surface charges of MOF samples were determined by using a Zeta potential analysis (Nano ZSE, Malvern, UK). The thermal stability of the MOF was analyzed using a thermogravimetric analyzer under nitrogen atmosphere, TGA 4000 (PerkinElmer, Waltham, MA).

Characterization of pristine and PES/PDA@Ce-MOF membranes

The morphology (top, bottom, and cross-sectional areas), elemental composition, and functionalization of the fabricated membranes were also assessed by the Quanta FEG 250 and Bruker ATR FT-IR instruments. To obtain cross-sectional SEM images of the membrane samples, small pieces of membrane

samples were immersed in liquid nitrogen for 30 s and carefully fractured. The tensile strength of the pristine and composite membranes was determined with a universal strength testing machine, Instron 5966 (Instron, USA). The measurements were done while applying a strain rate of 5 mm/min until fracture. The topography and surface roughness of the composite membranes were assessed using an atomic force microscope, MFP-3D Origin AFM (Asylum Research, Santa Barbara, CA). The membrane samples were analyzed via non-contact mode using a Si tip with a frequency of 63.5 kHz (Ted Pella, Redding, CA). The scan area taken for all membranes was 2 μm × 2 μm.

The static contact angles of DI water were measured by the sessile drop method using Krüss GmbH drop shape analyzer using 5 μL DI water droplets ejected via a micro-syringe. Measurements were taken at 5 different surface areas and average values were reported⁴⁵. The surface free energy ($-\Delta G_{SL}$) was calculated using the below Young-Dupre equation (Eq. (1))⁵

$$-\Delta G_{SL} = (1 + \cos \theta) \gamma_L^T \quad (1)$$

where θ is the DI water contact angle and γ_L^T is the water surface tension constant (72.8 mJ.m⁻²).

At three different pH levels (5, 7, and 9), the zeta potential value of prepared membranes was determined using the Anton Paar SurPASSTM 3 electro-kinetic analyzer. Membrane porosity was determined via gravimetric method. Equal circular cuts of all membranes were prepared and soaked in DI water for 24 h and weighed. Then, the membranes were completely dried and weighed to record their dry weights. A digital micrometer (Mitutoyo, Japan) was used to measure the thickness of the membranes. Equation (2) was used to calculate porosity⁴⁴:

$$\varepsilon = \frac{(W_w - W_d)}{A_m \delta \rho_g} \times 100 \quad (2)$$

where ε is the porosity (%), W_w and W_d are the wet and dry weights of the membranes (g), A_m is the membrane area (cm²), δ is the measured membrane thickness (cm), and ρ_g is the DI water density (0.998 g.cm⁻³).

The mean pore size was calculated using Guerout-Elford-Ferry equation (Eq. (3))¹³:

$$r_m = \sqrt{\frac{(2.9 - 1.75\varepsilon) \cdot 8\eta\delta Q}{\varepsilon A_m \Delta P}} \quad (3)$$

where r_m is the mean pore size (m), ε is the membrane porosity (%), η is the DI water viscosity (8.9 × 10⁻⁴ Pa.s), Q is the DI water flow (m³.s⁻¹), and ΔP is operating transmembrane pressure (Pa).

Membrane filtration performance

The pure water flux of the fabricated membranes was measured using a stirred dead-end filtration cell, UHP 4370 (Sterlitech Co., USA) with a membrane diameter of 40 mm. The UF setup includes a compressed nitrogen gas cylinder which was used to maintain a transmembrane pressure of 1 bar. All membranes were first compacted 30 min prior to measuring flux values. The pure water flux (J_w , LMH) was calculated by using DI water as feed and measuring the volume after 20 min using Eq. (4) as follows²⁴:

$$J_w = \frac{V}{(A_m \times t)} \quad (4)$$

where V is the DI water volume collected (L), A_m is the area of the membrane tested (m²), and t is the time elapsed (h).

The separation performance of the membranes was then studied using BSA protein with a feed concentration of 100 ppm. To prepare 1 L of BSA solution, 1.19 g and 1.40 g of sodium dihydrogen phosphate and sodium phosphate dibasic were added and stirred in 1 L of DI water for 1 h. The pH was then measured to be 7.0. Then, 100 mg of BSA was added to the

prepared 10 mM phosphate buffer solution and stirred for another hour. The BSA feed solution was filtered through the membrane at an operating pressure of 1 bar. The concentration of BSA was determined via a UV-Visible spectrophotometer, UV-1800 (Shimadzu, Japan) at a wavelength of 280 nm, after which the rejection (R) was calculated using Eq. (5):

$$R = \frac{C_f - C_p}{C_f} \times 100 \quad (5)$$

where C_f and C_p are the feed and permeate concentrations (ppm), respectively.

Using the same filtration cell discussed above, 50 ppm humic acid solutions were filtered through pristine and MOF-modified membranes to determine the separation performance of humic acid (HA). BSA and HA filtration procedures were followed in the same manner. Using a UV-Vis spectrometer (UV-1800 Shimadzu, Japan) at a wavelength of 254 nm, the concentration of HA in the feed and permeate after filtration was determined. The HA flux and rejection performance of membranes was calculated using Eq. (4) and Eq. (5).

Flux recovery ratio (FRR), reversible (R_r), and irreversible (R_{ir}) fouling ratios were calculated using Eqs. (6–8) to study the antifouling properties of the membranes through five cycles of BSA filtration where hydraulic washing took place in between cycles⁵.

$$FRR = \frac{J_{w_n}}{J_{w_{n-1}}} \times 100 \quad (6)$$

$$R_r = \frac{J_{w_n} - J_{BSA}}{J_{w_{n-1}}} \times 100 \quad (7)$$

$$R_{ir} = \frac{J_{w_{n-1}} - J_{w_n}}{J_{w_{n-1}}} \times 100 \quad (8)$$

where $J_{w_{n-1}}$ indicates the water flux in the $(n-1)^{th}$ cycle ($Lm^{-2}h^{-1}$); J_{w_n} is the water flux in the n^{th} cycle ($Lm^{-2}h^{-1}$) after hydraulic cleaning; and J_{BSA} is the BSA solution flux ($Lm^{-2}h^{-1}$).

DATA AVAILABILITY

All data generated or analyzed during this study are included in this published article and its supplementary information files.

Received: 15 September 2023; Accepted: 23 January 2024;

Published online: 08 February 2024

REFERENCES

- Mukhopadhyay, A., Duttagupta, S. & Mukherjee, A. Emerging organic contaminants in global community drinking water sources and supply: a review of occurrence, processes and remediation. *J. Environ. Chem. Eng.* **10**, 107560 (2022).
- Al Aani, S., Mustafa, T. N. & Hilal, N. Ultrafiltration membranes for wastewater and water process engineering: a comprehensive statistical review over the past decade. *J. Water Process Eng.* **35**, 101241 (2020).
- Shoshaa, R., Ashfaq, M. Y. & Al-Ghouti, M. A. Recent developments in ultrafiltration membrane technology for the removal of potentially toxic elements, and enhanced antifouling performance: a review. *Environ. Technol. Innov.* **31**, 103162 (2023).
- Kallem, P., Ibrahim, Y., Hasan, S. W., Show, P. L. & Banat, F. Fabrication of novel polyethersulfone (PES) hybrid ultrafiltration membranes with superior permeability and antifouling properties using environmentally friendly sulfonated functionalized polydopamine nanofillers. *Sep. Purif. Technol.* **261**, 118311 (2021).
- Arumugham, T. et al. Surface-engineered polyethersulfone membranes with inherent Fe–Mn bimetallic oxides for improved permeability and antifouling capability. *Environ. Res.* **204**, 112390 (2022).
- Li, N. et al. MXene-PANI/PES composite ultrafiltration membranes with conductive properties for anti-fouling and dye removal. *J. Membr. Sci.* **668**, 121271 (2023).
- Nie, Z. et al. Dopamine-triggered one-step codeposition of zwitterionic surfactants for anti-fouling polyethersulfone ultrafiltration membrane modification. *Appl. Surf. Sci.* **598**, 153871 (2022).
- Yadav, A., Singh, K. & Shahi, V. K. Side-chain grafted functional groups poly(vinylidene fluoride-hexafluoropropylene) anti-fouling fluorinated polymer membrane with tuneable hydrophobicity for distillation. *Desalination* **525**, 115501 (2022).
- Yan, L. et al. Bio-inspired mineral-hydrogel hybrid coating on hydrophobic PVDF membrane boosting oil/water emulsion separation. *Sep. Purif. Technol.* **285**, 120383 (2022).
- Zhang, W., Huang, H. & Bernstein, R. Zwitterionic hydrogel modified reduced graphene oxide/ZnO nanocomposite blended membrane with high antifouling and antibiofouling performances. *J. Colloid Interface Sci.* **613**, 426–434 (2022).
- Vatanpour, V. et al. Application of g-C₃N₄/ZnO nanocomposites for fabrication of anti-fouling polymer membranes with dye and protein rejection superiority. *J. Membr. Sci.* **660**, 120893 (2022).
- Rahimi, A. & Mahdavi, H. Zwitterionic-functionalized GO/PVDF nanocomposite membranes with improved anti-fouling properties. *J. Water Process Eng.* **32**, 100960 (2019).
- Arumugham, T., Amimodu, R. G., Kaleekkal, N. J. & Rana, D. Nano CuO/g-C₃N₄ sheets-based ultrafiltration membrane with enhanced interfacial affinity, anti-fouling and protein separation performances for water treatment application. *J. Environ. Sci.* **82**, 57–69 (2019).
- Gholami, F., Zinadini, S. & Zinatizadeh, A. A. Preparation of high performance CuBTC/PES ultrafiltration membrane for oily wastewater separation; A good strategy for advanced separation. *J. Environ. Chem. Eng.* **8**, 104482 (2020).
- Kumar, S. et al. Green synthesis of metal-organic frameworks: a state-of-the-art review of potential environmental and medical applications. *Coord. Chem. Rev.* **420**, 213407 (2020).
- Ghanbari, T. & Abnisa, F. & Daud, W. M. A. W. A review on production of metal organic frameworks (MOF) for CO₂ adsorption. *Sci. Total Environ.* **707**, 135090 (2020).
- Al-Shaeli, M. et al. Long-term stable metal organic framework (MOF) based mixed matrix membranes for ultrafiltration. *J. Membr. Sci.* **635**, 119339 (2021).
- Ren, Y. et al. MIL-PVDF blend ultrafiltration membranes with ultrahigh MOF loading for simultaneous adsorption and catalytic oxidation of methylene blue. *J. Hazard. Mater.* **365**, 312–321 (2019).
- Rameesha, L., Rana, D. & Nagendran, A. Fabrication and characterization of poly(vinylidene fluoride) hybrid ultrafiltration membranes with silver loaded MOF-5 for enhanced permeation, antifouling and antibiofouling performance. *J. Environ. Chem. Eng.* **11**, 109888 (2023).
- Samari, M., Zinadini, S., Zinatizadeh, A. A., Jafarzadeh, M. & Gholami, F. Designing of a novel polyethersulfone (PES) ultrafiltration (UF) membrane with thermal stability and high fouling resistance using melamine-modified zirconium-based metal-organic framework (UiO-66-NH₂/MOF). *Sep. Purif. Technol.* **251**, 117010 (2020).
- Sun, H., Tang, B. & Wu, P. Hydrophilic hollow zeolitic imidazolate framework-8 modified ultrafiltration membranes with significantly enhanced water separation properties. *J. Membr. Sci.* **551**, 283–293 (2018).
- Zhao, J. et al. MOF@Polydopamine-incorporated membrane with high permeability and mechanical property for efficient fouling-resistant and oil/water separation. *Environ. Res.* **236**, 116685 (2023).
- Ren, H.-M. et al. Proton conductive lanthanide-based metal-organic frameworks: synthesis strategies, structural features, and recent progress. *Top. Curr. Chem.* **380**, 9 (2022).
- Mohammadnezhad, F., Feyzi, M. & Zinadini, S. A novel Ce-MOF/PES mixed matrix membrane; synthesis, characterization and antifouling evaluation. *J. Ind. Eng. Chem.* **71**, 99–111 (2019).
- Liang, Z. et al. Composite PVDF ultrafiltration membrane tailored by sandwich-like GO@UiO-66 nanoparticles for breaking the trade-off between permeability and selectivity. *Sep. Purif. Technol.* **276**, 119308 (2021).
- Metilli, L., Ugo, H., Chèvremont, W., Picard, C. & Pignon, F. Self-supported MOF/cellulose-nanocrystals materials designed from ultrafiltration. *Soft Matter* **19**, 8228–8239 (2023).
- Li, R. et al. Inkjet printing of dopamine followed by UV light irradiation to modify mussel-inspired PVDF membrane for efficient oil-water separation. *J. Membr. Sci.* **619**, 118790 (2021).
- Kallem, P. et al. High-performance thin-film composite forward osmosis membranes with hydrophilic PDA@TiO₂ nanocomposite substrate for the treatment of oily wastewater under PRO mode. *J. Environ. Chem. Eng.* **10**, 107454 (2022).
- Shen, J. et al. Polydopamine modified cerium-based MOFs/ chitosan aerogel beads for the efficient phosphate removal. *Chemosphere* **345**, 140421 (2023).
- Yang, S., Zou, Q., Wang, T. & Zhang, L. Effects of GO and MOF@GO on the permeation and antifouling properties of cellulose acetate ultrafiltration membrane. *J. Membr. Sci.* **569**, 48–59 (2019).
- Kuila, A. et al. Improved charge carrier dynamics through a type II staggered Ce MOF/mc BIV04 n-n heterojunction for enhanced visible light utilisation. *Appl. Surf. Sci.* **553**, 149556 (2021).

32. Ashrafzadeh Afshar, E. et al. Magnetic nanoparticles based on cerium MOF supported on the MWCNT as a fluorescence quenching sensor for determination of 6-mercaptopurine. *Environ. Pollut.* **305**, 119230 (2022).
33. Sangeetha, S. & Krishnamurthy, G. Electrochemical and photocatalytic applications of Ce-MOF. *Bull. Mater. Sci.* **43**, 269 (2020).
34. Sun, D. et al. Polydopamine coated Co₂(OH)2BDC nanosheets for anticorrosive reinforcement of water-borne epoxy coating. *Prog. Org. Coat.* **175**, 107368 (2023).
35. He, J. et al. The structural design and valence state control of cerium-based metal-organic frameworks for their highly efficient phosphate removal. *J. Clean. Prod.* **321**, 128778 (2021).
36. Kasemset, S., He, Z., Miller, D. J., Freeman, B. D. & Sharma, M. M. Effect of polydopamine deposition conditions on polysulfone ultrafiltration membrane properties and threshold flux during oil/water emulsion filtration. *Polymer* **97**, 247–257 (2016).
37. Bai, L. et al. Surface coating of UF membranes to improve antifouling properties: a comparison study between cellulose nanocrystals (CNCs) and cellulose nanofibrils (CNFs). *Chemosphere* **217**, 76–84 (2019).
38. Zangeneh, H., Rahimi, Z., Zinatizadeh, A. A., Razavizadeh, S. H. & Zinadini, S. I-Histidine doped-TiO₂-CdS nanocomposite blended UF membranes with photocatalytic and self-cleaning properties for remediation of effluent from a local waste stabilization pond (WSP) under visible light. *Process Saf. Environ. Prot.* **136**, 92–104 (2020).
39. Abdulkarem, E., Ibrahim, Y., Naddeo, V., Banat, F. & Hasan, S. W. Development of Polyethersulfone/ α -Zirconium phosphate (PES/ α -ZrP) flat-sheet nanocomposite ultrafiltration membranes. *Chem. Eng. Res. Des.* **161**, 206–217 (2020).
40. Mahlangu, O. T., Mamba, G. & Mamba, B. B. A facile synthesis approach for GO-ZnO/PES ultrafiltration mixed matrix photocatalytic membranes for dye removal in water: leveraging the synergy between photocatalysis and membrane filtration. *J. Environ. Chem. Eng.* **11**, 110065 (2023).
41. Zhang, P., Xu, Q., Li, X. & Wang, Y. pH-responsive polydopamine nanoparticles for photothermally promoted gene delivery. *Mater. Sci. Eng. C* **108**, 110396 (2020).
42. Chu, Z., Chen, K., Xiao, C., Ling, H. & Hu, Z. Performance improvement of polyethersulfone ultrafiltration membrane containing variform inorganic nano-additives. *Polymer* **188**, 122160 (2020).
43. Yassin, J. M., Taddesse, A. M. & Sánchez-Sánchez, M. Room temperature synthesis of high-quality Ce(IV)-based MOFs in water. *Microporous Mesoporous Mater.* **324**, 111303 (2021).
44. Hegab, H. M. et al. Designing of amino silica covalently functionalized carboxylic multi-wall carbon nanotubes-based polyethersulfone membranes for enhancing oily wastewater treatment. *J. Environ. Chem. Eng.* **10**, 108667 (2022).
45. Ghiasi, S., Behboudi, A., Mohammadi, T. & Khanlari, S. Effect of surface charge and roughness on ultrafiltration membranes performance and polyelectrolyte nanofiltration layer assembly. *Colloids Surf. Physicochem. Eng. Asp.* **580**, 123753 (2019).
46. Mansor, E. S., Ali, E. A. & Shaban, A. M. Tight ultrafiltration polyethersulfone membrane for cheese whey wastewater treatment. *Chem. Eng. J.* **407**, 127175 (2021).
47. Gowriboy, N., Kalaivizhi, R., Kaleekkal, N. J., Ganesh, M. R. & Aswathy, K. A. Fabrication and characterization of polymer nanocomposites membrane (Cu-MOF@CA/PES) for water treatment. *J. Environ. Chem. Eng.* **10**, 108668 (2022).

ACKNOWLEDGEMENTS

The authors extend their gratitude to the Center for Membranes and Advanced Water Technology (CMAT) at Khalifa University in Abu Dhabi, United Arab Emirates (UAE), for providing research funding through grant number RC2-2018-009.

AUTHOR CONTRIBUTIONS

Dana Kadadou: experimental, data curation, visualization, writing-original draft, review and editing. Thanigaivelan Arumugham: conceptualization, experimental, data curation, data manipulation, visualization, writing-original draft, review and editing, validation. Lina Tizani: data curation, data manipulation, and visualization. Shadi W. Hasan: conceptualization, validation, writing—review and editing, and funding acquisition.

COMPETING INTERESTS

The authors declare no competing interests.

ADDITIONAL INFORMATION

Supplementary information The online version contains supplementary material available at <https://doi.org/10.1038/s41545-024-00302-z>.

Correspondence and requests for materials should be addressed to Shadi W. Hasan.

Reprints and permission information is available at <http://www.nature.com/reprints>

Publisher's note Springer Nature remains neutral with regard to jurisdictional claims in published maps and institutional affiliations.



Open Access This article is licensed under a Creative Commons Attribution 4.0 International License, which permits use, sharing, adaptation, distribution and reproduction in any medium or format, as long as you give appropriate credit to the original author(s) and the source, provide a link to the Creative Commons license, and indicate if changes were made. The images or other third party material in this article are included in the article's Creative Commons license, unless indicated otherwise in a credit line to the material. If material is not included in the article's Creative Commons license and your intended use is not permitted by statutory regulation or exceeds the permitted use, you will need to obtain permission directly from the copyright holder. To view a copy of this license, visit <http://creativecommons.org/licenses/by/4.0/>.

© The Author(s) 2024